ADVANCED OPTICAL MATERIALS
www.advopticalmat.de

Anisotropic Resistivity Surfaces Produced in ITO Films by Laser-Induced Nanoscale Self-organization

Carmen Lopez-Santos, Daniel Puerto, Jan Siegel, Manuel Macias-Montero, Camilo Florian, Jorge Gil-Rostra, Víctor López-Flores, Ana Borras, Agustín R. González-Elipe, and Javier Solis**

Highly anisotropic resistivity surfaces are produced in indium tin oxide (ITO) films by nanoscale self-organization upon irradiation with a fs-laser beam operating at 1030 nm. Anisotropy is caused by the formation of laser-induced periodic surface structures (LIPSS) extended over cm-sized regions. Two types of optimized structures are observed. At high fluence, nearly complete ablation at the valleys of the LIPSS and strong ablation at their ridges lead to an insulating structure in the direction transverse to the LIPSS and conductive in the longitudinal one. A strong diminution of In content in the remaining material is then observed, leading to a longitudinal resistivity $\rho_L \approx 1.0\ \Omega\cdot$cm. At a lower fluence, the material at the LIPSS ridges remains essentially unmodified while partial ablation is observed at the valleys. The structures show a longitudinal conductivity two times higher than the transverse one, and a resistivity similar to that of the pristine ITO film ($\rho \approx 5 \times 10^{-4}\ \Omega\cdot$cm). A thorough characterization of these transparent structures is presented and discussed. The compositional changes induced as laser pulses accumulate, condition the LIPSS evolution and thus the result of the structuring process. Strategies to further improve the achieved anisotropic resistivity results are also provided.

1. Introduction

Transparent conducting oxides (TCOs) are materials with a comparably low optical absorption in the visible region of the spectrum which makes them particularly suitable for applications in the fields of information technology (organic light emitting diodes, flat panel displays, etc.) and energy harvesting (photovoltaics, low emissivity coatings, etc.).[1] They are produced by creating electron degeneracy in a wide bandgap oxide either introducing non-stoichiometry (solid solutions) and/or appropriate dopants, like Sb or F.[2] This is usually achieved in mixtures of different Group III oxides with metal oxides where the metal can be a part of the semiconductor oxide or act as dopant. This leads to different families of TCOs including AZO (aluminum zinc oxide), IZO (indium zinc oxide), ITO (indium tin oxide), GZO (gallium zinc oxide), and so on. Among them ITO (typically ≈90% wt% In_2O_3 + 10 wt% SnO_2) plays a key role, especially to produce transparent conductive electrodes (TCEs) in flat-panel displays.

Regarding the structuring of ITO films, although wet chemical etching is suitable for producing micron-width electrodes, the need for rapid, and mask-less patterning of large areas led to investigation of the use of laser structuring already in the late 90s.[3] A similarly important application of lasers for processing TCOs is their use for sintering spin-coated films formed by nanoparticles, especially on flexible substrates.[4–6]

However, the peculiarities of its absorption spectrum and the regular use of transparent substrates impose limitations in

Dr. C. Lopez-Santos, Dr. J. Gil-Rostra, Dr. V. López-Flores, Dr. A. Borras, Prof. A. R. González-Elipe
Nanotechnology on Surfaces Group
Instituto de Ciencia de Materiales de Sevilla (ICMS-US-CSIC)
Américo Vespucio 49, Seville 41092, Spain
E-mail: mclopez@icmse.csic.es

The ORCID identification number(s) for the author(s) of this article can be found under https://doi.org/10.1002/adom.202001086.

[+]Present address: Polytechnic School of University of Alicante, Spain

[++]Present address: Princeton Institute for the Science and Technology of Materials (PRISM), Princeton University, Princeton, NJ, USA

DOI: 10.1002/adom.202001086

Dr. C. Lopez-Santos
Departamento de Física Atómica, Molecular y Nuclear
Facultad de Física
Universidad de Sevilla
Reina Merdedes, s/n, Seville 41012, Spain

Dr. D. Puerto,[+] Dr. J. Siegel, Dr. M. Macias-Montero, Dr. C. Florian,[++]
Prof. J. Solis
Laser Processing Group (LPG)
Instituto de Óptica (IO-CSIC)
Serrano 121, Madrid 28006, Spain
E-mail: j.solis@io.cfmac.csic.es

the selection of laser wavelengths for ablative structuring in the vis–NIR.[7] This can be overcome by using UV wavelengths[8] or sacrificial absorbing layers.[9]

Alternatively, the use of ultrafast lasers in the ps- or fs-pulse regimes has been analyzed by several research groups,[9–12] leading in some cases to an improved performance.[13] This approach, when multi-pulse processing is used, has the additional consequence of generating laser-induced periodic surface structures (LIPSS),[14] an effect that has recently received attention due to its high potential for producing optical[15,16] or electrical anisotropies.[17,18] However, due to its long skin penetration depth in the vis–NIR, it is difficult to fabricate macroscopically continuous LIPSS[19,20] in ITO, a requirement for many practical applications. In what follows we provide a non-exhaustive summary of relevant results regarding LIPSS fabrication in ITO.

Ablative LIPSS aligned perpendicular to the laser beam polarization (⊥-LIPSS) and periods as small as $\approx\lambda/15$ have been observed in films irradiated with high repetition rate, fs laser pulses at 800 nm at extremely slow scanning speeds ($\approx 10'$s μm s^{-1}).[21] At a much lower repetition rate, Wang et al.[22] observed periodic arrangements of nanolines and nanodots with longer, multimodal period structures ($\Lambda \approx \lambda$, $\lambda/2$ and $\lambda/4$) in samples statically irradiated at the same wavelength. More recently, femtosecond-laser pulses at 1030 nm have been used to generate ablative ⊥-LIPSS with a very small period[16] ($\Lambda \approx \lambda/9$) using a slow beam scanning speed. Farid et al.[23] have reported on the evolution of LIPSS morphologies in static and moving samples. In the former, they observed after a few pulses ⊥-LIPSS to develop. For further pulse accumulation, LIPSS parallel to the laser beam polarization (∥-LIPSS) coexisting with ⊥-LIPSS were observed while at even higher pulse numbers ($N > \approx 20$), ∥-LIPSS predominate. However, upon film scanning during laser exposure, ∥-LIPSS were never observed, and a bimodal distribution of ⊥-LIPSS ($\Lambda \approx \lambda/2$ and $\approx\lambda$, $\lambda = 532$ nm) occurred instead. At the same time, these authors observed Λ values in the ≈100–500 nm range, depending on the local fluence. The transition from low spatial frequency (LSF) to high spatial frequency (HSF) LIPSS with the laser scan speed has been reported by Liu and coworkers[24] upon ps-laser irradiation at 1064 nm, and attributed to splitting phenomena.[25] LSF-LIPSS formation upon nanosecond-laser pulsed irradiation has also been recently reported at 532 nm.[26] Such a rich phenomenology further spans when considering the interaction of the laser with initially amorphous ITO films[27] where amorphous-crystalline, ⊥ HSF-LIPSS have been observed.

For what concerns functionality, thin ITO films irradiated with fs-laser pulses develop a strong form birefringence ($|\Delta n| \approx 0.2$) related to deeply ablated ⊥-LIPSS ($\Lambda \approx \lambda/9$) formed upon slow sample scanned irradiation.[16] The same structures were subsequently used for liquid crystal alignment layers.[18] More recently, a hybrid approach combining direct laser interference patterning (DLIP) and LIPSS has been used to produce anisotropic conductance structures.[17] The LIPSS period found ($\Lambda \approx 75$ nm $\approx \lambda/4$) was over-imposed to the DLIP periodicity leading to a conductance anisotropy of $\approx 50 \times 10^3$, as measured by two-point probing measurements. Unfortunately, quantitative resistivity measurements were provided only for the as-deposited films (≈24 Ω sq^{-1}) that also showed a relatively large transmission in the near IR of about 70% at 2 μm. This makes it difficult to assess the chemical/structural origin of the induced changes.

In this work, we report the production of surfaces with high anisotropic resistivity in ITO films, reaching electrical insulation along one axis and electrical conductance in the transversal one. Such a strong anisotropy effect is caused by the formation of coherently extended, LSF-LIPSS upon fs-laser irradiation at 1030 nm. After optimization of the laser processing parameters, two main types of anisotropic resistivity structures have been produced based on either strong ablation and material compositional changes, or gentle ablation. These structures have been thoroughly characterized in terms of morphology, composition, structure, optical properties, and resistivity. The origin of their electrical and optical response is discussed in terms of the compositional and structural evolution of the irradiated material. Feasible routes to further improve their anisotropic performance are presented.

2. Results and Discussion

2.1. Morphology of the Irradiated Surfaces

Figure 1 gathers several morphological images of two optimized structures induced at different fluences (0.64 and 0.89 J cm^{-2}). The laser repetition rate used in this case was 500 kHz and the laser beam polarization was perpendicular to the scan direction. The spot size at the sample was 10.2 μm ($1/e^2$ intensity decay). A scan speed of 2 m s^{-1}, and a scan line separation of 4 μm were used. The images show the formation of LIPSS, and correspond to the narrow fluence interval where coherent propagation of LSF-LIPSS[19,20] can be successfully induced. The preservation of the alignment of the structures over a long distance (up to 1 cm) can be well appreciated in the low magnification optical images in the figure. From now on, we will refer to them as LF (low fluence) and HF (high fluence) structures.

There is though a large variability in the morphology of the samples depending on the processing parameters, as shown in the Supporting Information. In general, fluences above 1 J cm^{-2} lead to splitting of the LSF-LIPSS in structures showing $\Lambda \approx \lambda/2$ (cf. Figure S1, Supporting Information) or the coexistence of both $\Lambda \approx \lambda$ and $\Lambda \approx \lambda/2$ periods (cf. Figure S2c, Supporting Information). Such a splitting phenomenon has been reported in ITO films upon irradiation with both ps- and fs-laser pulses,[22–24] and attributed to progressive compositional[22] or surface roughness changes[24,25] during the structure evolution. Yet, none of these works has reported the homogeneous formation of single period, LSF-LIPSS, like those shown in Figure 1.

As can be appreciated in the SEM and AFM images, the structures show periods close to λ ($\Lambda \approx 940$ and 890 nm, respectively, for the LF and HF samples). The narrow width and large depth of the valleys in the LF structures lead to tip-angle related artifacts yielding artificially low values in the modulation depth derived from AFM measurements. This value has been thus estimated to be ≈350 nm by using interferometric microscopy and SEM cross-section analysis as shown in the insets in Figure 1, while the thickness of the film underneath the valleys is ≈150 nm (cf. Figure S3, Supporting Information). This indicates that at the ridges of the LF structures, ablation effects are very small. For the HF sample, interferometric microscopy and SEM cross-section measurements show instead, a strong diminution of the overall film thickness caused by ablation. The depth of

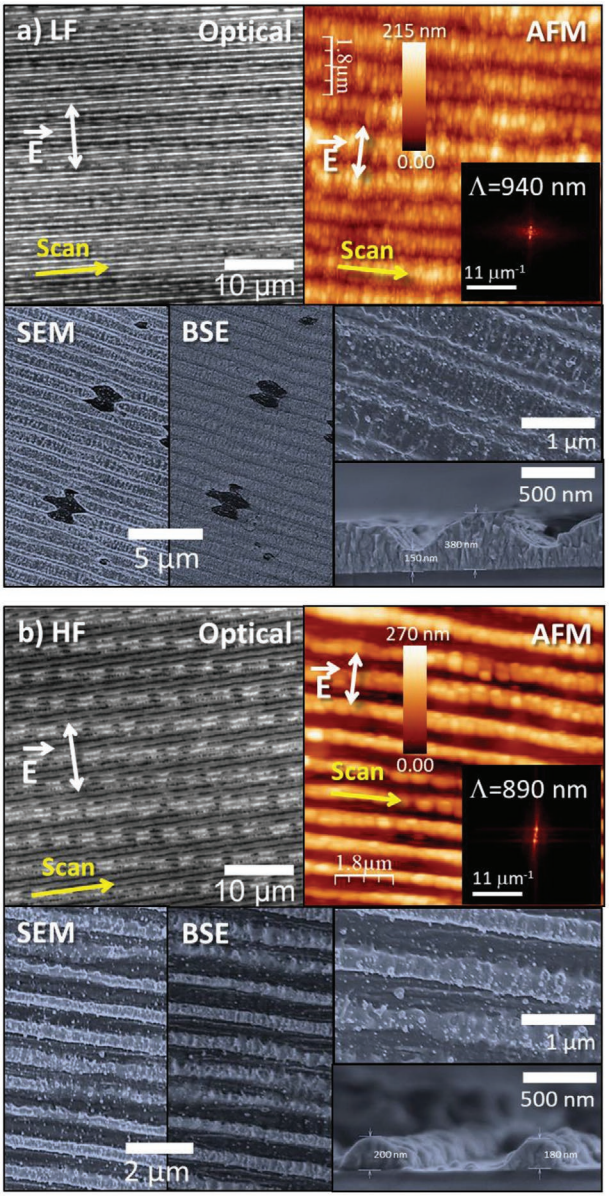

Figure 1. Morphological surface analysis of LIPSS generated in a) the LF sample and b) the HF sample. Characterization by optical (top left) and AFM (top right) microscopies, and SEM in BSE (bottom middle) and SE (bottom left and right) modes, this latter at two different magnifications. SE-SEM images of the cross-section of samples at LIPSS normal direction, showing the topography of the laser-irradiated samples, have also been included (bottom right). The laser beam polarization and scan directions are indicated as white and yellow colored lines in the optical and AFM microscopy images. The spatial scale is included in all images. In each AFM image, the inset shows its FFT.

modulation observed on average (≈180 nm) is smaller than in the LF case while the thickness of the film remaining at the valleys, most likely discontinuous, is estimated to be below ≈10 nm, where the fact that the valleys of the HF sample are discontinuous can be clearly appreciated by SEM cross-section analysis.

The AFM measurements of the LF structures also show the presence of a sub-wavelength pattern ($\Lambda \approx 400$ nm) aligned parallel to the electric field of the laser. Inside this pattern, a finer periodicity (≈150 nm) is often observed, a value close to the lowest ones reported.[16] Such short periods were observed upon fs-laser irradiation at a much lower scanning speed (≈1 mm s^{-1}) and the LIPSS were oriented perpendicular to the laser polarization instead. In our case, these fine HSF-LIPSS are also observed at the edges of the overlap regions of consecutive scans when the polarization is parallel to the scan direction (cf. Figure S2a, Supporting Information). The transition from LIPSS perpendicular to parallel to the laser electric field has been reported upon static irradiation of ITO films by Farid and coworkers,[23] and attributed to the formation of nanoblisters in the LIPSS initially perpendicular to the field generating an uneven fluence profile on the surface.

The depth modulation of the structures can also be appreciated in the SEM images shown in Figure 1. At LF, the structures consist of broad ridges (≈700 nm broad) alternating with narrower (≈240 nm) valleys surrounded by molten rims. The broad maxima also show (cf. zoom inset) the presence of the already indicated fine modulation ($\Lambda \approx \lambda/2$) aligned parallel to the laser polarization, as well as very small molten droplets, indicative of liquid phase splashing at the ablated channels. The BSE image shows instead a rather homogeneous contrast, with a darker appearance at the valleys. This suggests the occurrence of local compositional changes (Z-contrast) apparently stronger in the channels. For the HF case, the SEM images confirm the broader width of the valleys (≈600 nm) compared to the ridges (≈300 nm) (cf. zoomed inset). The BSE images indicate here a strong compositional difference between the material at the ridges and the valleys of the structure. Clear signs of re-solidification are also observed along with bigger molten droplets everywhere on the surface.

2.2. Compositional Changes

Figure 2 includes EDX compositional data from measurements at different regions of the LF and HF samples. For the LF case, the EDX spectra show clearly the L_α emission bands of In and Sn along with a small contribution of the K_α band of Si, associated with the fused silica substrate. This contribution, in the case of the non-treated material (unexposed, U-ITO), is comparable to the one observed at the ridges of the LF structure which suggests, as already indicated, a very small thickness diminution. The contributions of C, N, and O can also be appreciated in the low energy region (<1 eV) of the spectrum. The compositional maps show an In and Sn content homogeneously distributed over the ridges of the LF sample, and a decrease in the content of both elements at the valleys. Si is there observed, while the Si-peak appreciably increases in the EDX spectra consistently with the smaller film thickness of the structure. More importantly, the Sn/In cps. ratio increases (≈20%) at the valleys compared to the ridges, indicating a preferential loss of In at the regions experiencing the highest local fluence. The ratio observed at the ridges is similar to the one in non-irradiated regions.

In the HF case, the induced compositional changes are much stronger. The compositional maps show that In and Sn have been nearly completely removed at the valleys while broad Si stripes can noticeably be seen there. Consistently, the EDX

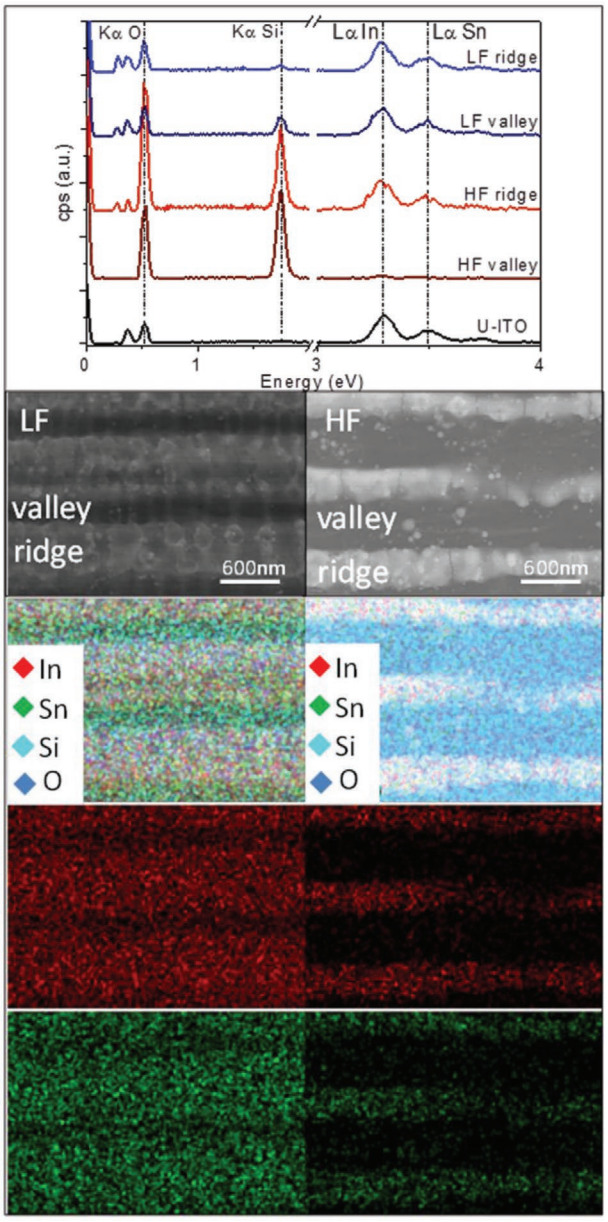

Figure 2. EDX analysis of the LF and HF samples. The EDX spectra shown correspond to the valleys and ridges of the structures, as indicated in the SEM images below. The colored images are compositional maps of the spatial distribution of the indicated elements. A spectrum of the unexposed surface (U-ITO) is also included.

spectrum shows a very strong contribution of Si and a nearly negligible contribution of In and Sn. At the ridges, the Sn/In cps. ratio is similar to the one observed at the valleys in the LF structures, while the Si and O peaks prevail in the spectrum.

The comparison of our results with previously reported works indicates that upon multi-pulse irradiation, the effect of the laser energy in the material progressively changes as pulses are accumulated. ITO films show an absorption coefficient at 1030 nm around 10^4 cm^{-1}[7,12] that leads to a single pulse ablation fluence of ≈9 J cm^{-2} for a similar pulse duration and film thickness.[9] We have observed LIPSS formation at 500 kHz pulse repetition rate, for fluences of just 0.5 J cm^{-2} at processing speed of 1 m s^{-1} (equivalent to ≈10 shots per spot). This value is ≈20 times smaller than that reported in ref. [12].

It is thus clear that although free carrier absorption initiates the deposition of laser energy in the film, the compositional changes occurring after each pulse progressively modify the material response. Indeed, compositional effects upon multi-pulse, fs-laser irradiation have already been pointed out by Wang et al.[22] who attributed the evolution of the electrical properties of irradiated films to the breaking of In—O and Sn—O bonds and the formation of metallic In—In clusters. Similarly, Farid et al.[23] have proposed the formation of In-rich nanoblisters as the trigger agent for LIPSS formation in ITO.

The compositional changes induced in the ITO films have also been analyzed by XPS spectroscopy in pristine[28] and laser-treated samples. The XPS spectra corresponding to the Sn3d, In3d, O1s, and Si2p bands are included in the Supporting Information (cf. Figure S4, Supporting Information) and show relevant differences only between non-irradiated and the HF samples. In the HF case, the appearance of the Si2p peak at ≈102 eV (corresponding to Si—O—Si and Si—OH bonds) and an additional contribution in the O1s spectrum at ≈532 eV, evidence that film at the valleys of the HF structures is nearly completely removed. A small shift to lower energies (≈0.2 eV) in the two 3d peaks of Sn and In with respect to the non-irradiated material is also observed. The small magnitude of the spectral shift and its narrower width allow discarding the formation of In—In bonds (In^0 bonding in the metallic state, metallization of the near-surface) as responsible for the shift, unlike the observations by Wang et al.[22] for a much higher accumulated laser dose.

Table 1 shows the composition of unexposed and irradiated regions derived from the XPS data. When comparing these values to the EDX characterization, it must be considered that XPS provides compositional values corresponding to an exponentially decaying interaction in the near-surface region (2–3 nm depth), which is a 2D average covers regions (ridges and valleys) with different compositions and spreads. The LF sample shows a small relative diminution of In (≈7%) and a clear increase of Sn (≈30%) content, leading to a significant increase in the Sn/In ratio. The EDX compositional data indicate though that the Sn/In ratio remains essentially unmodified at the broad ridges of the LF structures and increases at the valleys. These observations suggest that the preferential loss of In mainly occurs at the valleys of the LF structures.

The situation is different in the HF structures, where the ITO film is nearly completely removed at the valleys, and therefore the XPS-determined composition corresponds to the

Table 1. Average compositions determined from XPS spectra recorded at the surface of unexposed (U-ITO), LF and HF irradiated films. The compositional values are given in terms of atomic % and have been normalized to 100%.

	In [at%]	Sn [at%]	O [at%]	Si [at%]	Sn/In
U-ITO	36.1	3.9	60.0	–	0.106
LF sample	33.6	5.1	61.3	–	0.154
HF sample	29.8	4.9	59.0	4.3	0.166

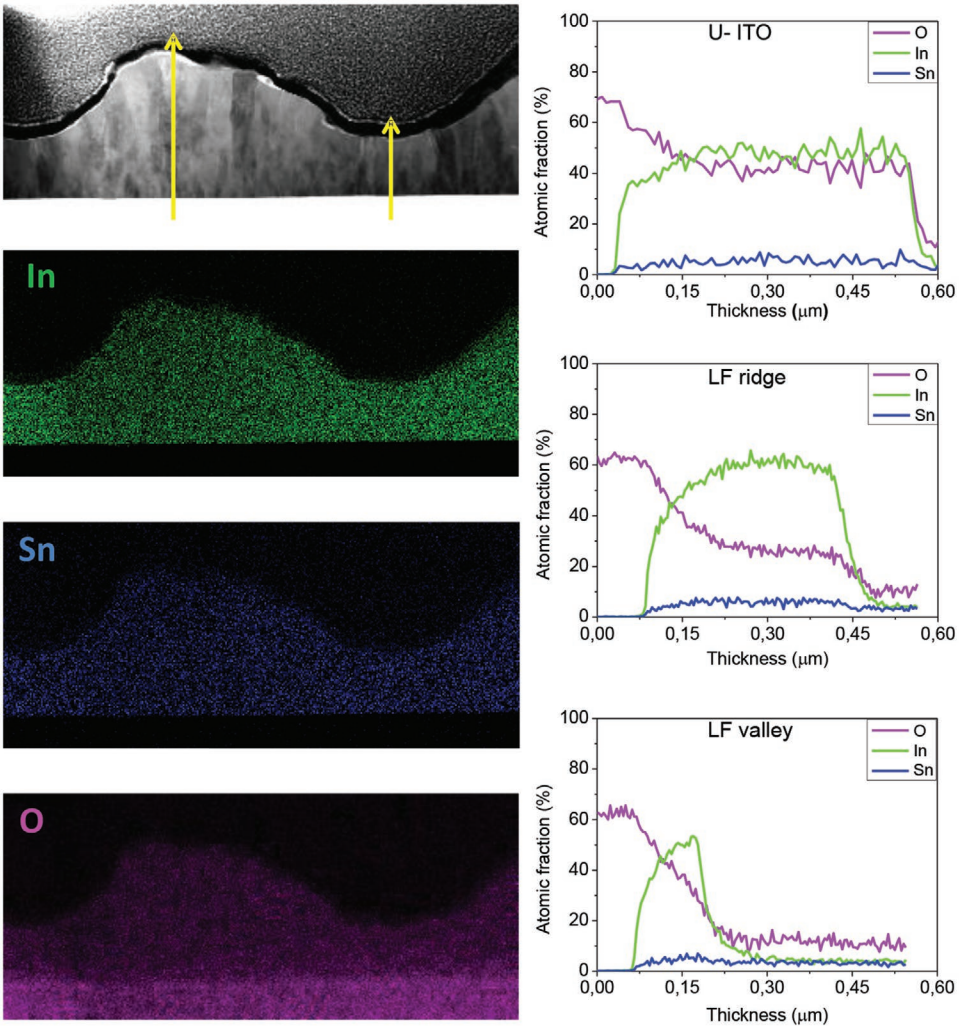

Figure 3. (left column) STEM/EDX analysis of an LF cross-section sample showing a high-resolution image of the structure across the LIPSS (top-left) and compositional maps associated with the In, Sn, and O distribution. (right column) Atomic fraction profiles through the substrate-film interface corresponding to a pristine sample (top-right), and a ridge (center-right) and a valley (bottom-right) of the LF sample. For these latter two, the scan line position is shown by the yellow lines in the STEM image.

material remaining at the ridges which, in agreement with the EDX data, shows a strong preferential loss of In.

In order to access the compositional changes occurring at the ridges and valleys of the LF-samples, thin lamellae of pristine and LF irradiated samples were produced by a Focused Ion Beam (FIB). The so produced cross-sectional samples were analyzed by EDX spectroscopy in a STEM. **Figure 3** shows a high-resolution image of a lamella cut normal to the LIPSS in an LF-sample along with several compositional maps. The quantified spatial distribution of In, Sn, and O (atomic fraction %) determined through a line perpendicular to the sample is included for the unexposed sample and at a ridge and a valley of the LF-sample

The STEM image clearly shows that the LF-irradiated structure is polycrystalline while the compositional maps show a relatively homogeneous distribution of the three elements, with a strong increase of the atomic fraction of oxygen at the vicinity of the boundary between the film and the substrate, this latter made of SiO_2. For the three in-depth compositional profiles, the position of the film interface can easily be determined by the sharp increase of the In content. The evolution of the oxygen content through the interface shows a progressive diminution over a transition region of ≈100 nm that can be attributed either to some residual oxygen diffusion, or to the interaction volume where the X-ray signal is produced (spatial resolution of the EDX probe), or both. Whatsoever the case, for a thickness above ≈200 nm over the interface the oxygen content stabilizes at a value (≈45 at%) smaller than that obtained through XPS measurements (≈60 at%). This is not surprising since in multicomponent compounds, especially in those including heavy elements, oxygen quantification by EDX is subjected to large uncertainties. In spite of this we can clearly see that both at the ridges and valleys of the structure, there is a diminution of oxygen in the film, something not apparent in the XPS measurements, more sensitive to the near-surface region.

Concerning the spatial distribution of In and Sn, the poor quantification of oxygen impedes making refined estimates to the In and Sn content/distribution. Still, we can see that the In

content at the ridges is very close to that of the pristine film, as we inferred too from the XPS data. The quantified In values at the center of the ridges (≈60 at%) are apparently above those measured in the non-irradiated film (50%), something that can only be attributed to the normalization procedure in the presence of oxygen losses. However, in the valleys, the maximum content of In computed by the EDX profiles at the STEM is clearly smaller than at the center of the ridges, while the Sn content remains nearly the same (≈5–6 at%) in both cases.

It seems clear that upon multiple pulse exposure of the films at fluences well below the single pulse ablation threshold,[12] as pulses accumulate, an increasing loss of In occurs, and most likely of oxygen too. EDX (at the SEM and STEM), and XPS measurements show a strong increase of the Sn/In ratio particularly in the regions experiencing the stronger local ablation effects. We can consider two plausible origins for the preferential loss of In: non-linear absorption and/or phase segregation effects. Wang et al.[22] have suggested that oxygen atoms in In_2O_3-like sites, adjacent to oxygen-deficient sites, might be vaporized by breaking In—O (bond strength ≈ 3.73 eV) and Sn—O (bond strength ≈ 5.68 eV) bonds[29] by multiphoton absorption. In such a scenario, the lower In-O bond strength would justify the preferential loss of In. Yet, even disregarding non-linear absorption, free carrier absorption may provide enough energy to melt the surface. Melting features are evident in the images in Figure 1, especially in the HF structures. Under these conditions, phase separation may locally occur leading to small amounts of segregated In_2O_3 and SnO_2 either due to rapid solidification effects and/or, if the preferential loss of In has sufficiently progressed, to a local concentration of SnO_2 exceeding its solubility limit in In_2O_3. Although crystalline In_2O_3 and SnO_2 are normally assumed to have a similar bandgap (≈3.7 eV[30,31]), several works have shown that the bandgap of In_2O_3 is smaller (≈3.0 eV[32]) and also that it shows a weak optical absorption onset at ≈2.6 eV.[33] Its lower absorption edge with respect to SnO_2 would further favor the preferential loss of In by multiphoton absorption upon phase segregation, and/or, most likely, by the non-stoichiometric, thermal decomposition of In_2O_3 with the release of In_2O (gas) at temperatures above 900 °C, as reported by de Wit.[34] A schematic picture of the processes associated with the preferential loss of In is included in **Figure 4**.

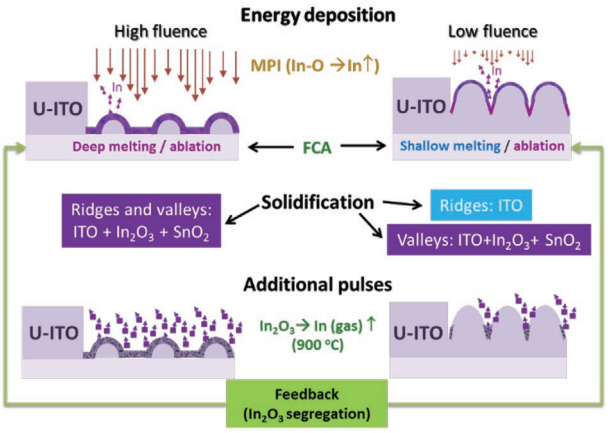

Figure 4. Schematic representation of the laser-ITO interaction process underlying the preferential loss of In in the HF and LF structures (see text).

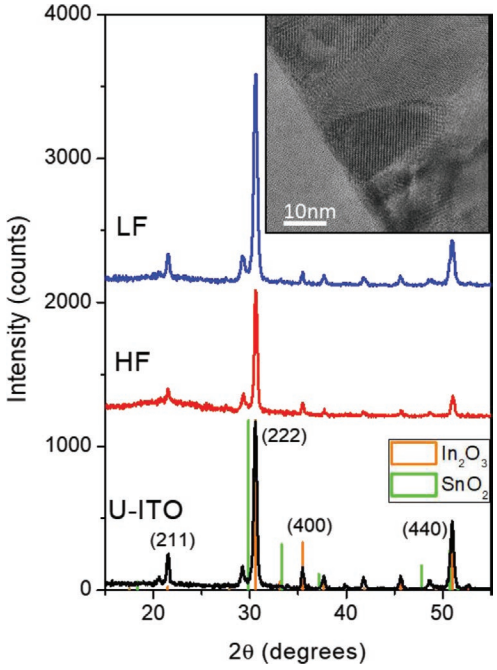

Figure 5. X-ray diffractograms of unexposed (U-ITO) films, and films irradiated at LF and HF. The position of the Bragg reflections corresponding to the crystallographic planes of In_2O_3 and SnO_2 is indicated with color lines. The inset shows a high-resolution STEM image of a cross-section of the LF-sample, confirming its polycrystalline nature.

2.3. Structure and Optical Properties of the Irradiated Surfaces

Figure 5 shows the X-ray diffraction patterns of LF and HF samples. As can be seen, in both cases, the ITO remaining at the surface is polycrystalline and the patterns can be indexed with the characteristic structure of the cubic phase of ITO. The (222) diffraction peak indicates the formation of In_2O_3 and $In_2Sn_yO_x$ polycrystalline domains while the broad band located around $2\theta \approx 20°$, visible only in the HF samples, corresponds to the amorphous SiO_2 contribution associated with the substrate.

The fact that polycrystalline material is formed upon irradiation is related to heat accumulation effects during processing at high repetition rates. These effects are stronger the higher the repetition rate and the higher the fluence.[35] Indeed, samples irradiated at lower fluence (i.e., 0.5 J cm^{-2}) or at higher fluence but lower repetition rate (i.e., 50 kHz) are amorphized upon processing (cf. Figure S5, Supporting Information). There is thus a relatively narrow fluence interval where LSF-LIPSS form and coherently propagate, while the irradiated material remains polycrystalline, a requirement to preserve the special near IR optical and conductivity properties of ITO.[36] When considering the beneficial effect of heat accumulation effects for annealing the generated structures to form polycrystalline material, it must be considered though, that an excessive laser dose can lead to cracking due to build-up thermal stresses and irregularities in the repetitive melting-solidification process. This may lead to discontinuities in the ridges of the structures, as observed in the HF samples, affecting their macroscopic conductivity, as it will be shown in Section 2.4.

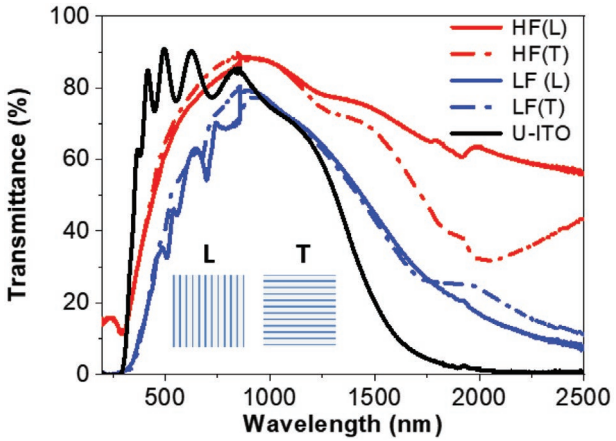

Figure 6. Optical transmission spectra at normal incidence (vis–NIR region) of the LF and HF samples with their LIPSS oriented longitudinally (L) or transversally (T) to the lines of the grating in the spectrophotometer, as indicated in the sketch of the inset. A spectrum of the unexposed material (U-ITO) has been included for reference.

The characteristic near-IR absorption of ITO is caused by the absorption of light by ionized states in the bandgap associated with two types of donor sites, oxygen vacancies [V_O''] and Sn^{+4} in substitutional positions [Sn´]. As a consequence, the material absorption in the IR strongly depends on its actual composition (oxygen and Sn/In stoichiometry),[37,38] which conditions the carrier density, and on its crystalline quality, which affects the carriers mobility (notice that Sn^{+4} does not contribute to conductivity in the amorphous phase[36]). The "optical window" for ITO is set thus at short wavelengths by its bandgap (≈3.75 eV) and at longer wavelengths by its plasma edge.

Figure 6 shows the optical transmittance spectra of the LF and HF samples when they are oriented with the LIPSS aligned longitudinally or transversally to the illumination beam axis. The transmission decrease observed in all cases in Figure 6 above 1000 nm is consistent with the polycrystalline nature of the processed surfaces (cf. Figure 5) and generally agrees with previous observations regarding the optical properties of polycrystalline ITO films.[39] Amorphous films upon processing are nearly transparent instead, with a spectrum very similar to that of un-doped In_2O_3[36] (cf. Figure S6, Supporting Information).

In general, higher crystalline quality surfaces, such as those in the LF samples, can reach near-IR transmission values close to those of the pristine films (see also Figure S6, Supporting Information). Indeed, the optical response of the material in the near IR strongly resembles that of the unexposed ITO, a feature suggesting a less severe impact of the laser-induced modifications in the density and mobility of carriers. Given the width and height of the ridge regions compared to the valleys, the global contribution to the material absorption in the LF sample must be dominated by the ridge regions that are compositionally very similar to the unexposed material. This is further confirmed by the appearance of a characteristic modulation in the L-spectrum of the LF-sample in the visible region. This modulation is similar to the one shown by the unexposed material and caused by interference effects in the spectral region where the film is transparent. This is clearly visible in the L-spectrum, where the structured film behaves as a nearly homogeneous thickness structure as seen by the illumination beam, and is blurred in the T-spectrum due to the alternation of high and low thickness regions contributing to interference phenomena.

The increased transparency observed in the HF sample in the 2000 nm region in both L and T spectra, compared to the pristine ITO film, implies changes in the carrier density/mobility of the material remaining at the surface. The Sn/In ratio at the ridges of the HF structures increases by at least 50% (cf. Table 1). According to the work by Maruyama and coworkers, this would lead to a reduction of the carrier mobility by at least a factor of two and, more importantly, to a diminution of the carrier density by more than one order of magnitude, to values ≈10^{20} cm^{-3}.[40] This would shift the cutoff plasma frequency deeper in the IR, generating the observed near-IR transmission increase with respect to the pristine film. These structures additionally show a strong dichroism in the near IR region around 2000 nm that can be well appreciated in Figure 6. The spectrum acquired in the T configuration shows a clear minimum at 2000 nm (dichroism), likely related to the combined effect of morphological and compositional changes when the LIPSS in the HF-sample are oriented transversally to the lines of the diffraction grating of the spectrophotometer. In our case, dichroism is only observed in the near IR region, unlike the coloration effects in the VIS region described in ref. [41], likely due to the shorter period there reported for the laser-induced structures.

There is an additional feature shared by HF and LF films: the diminution of transmission in the vicinity of the absorption edge (≈500 nm region) that bends to longer wavelengths. We believe that the changes observed close to the absorption edge are related to microstructural rather than compositional effects. For visible wavelengths, surface morphology also influences the transmission of ITO films due to grain boundary scattering.[37,42] After a series of severe melting-and-rapid solidification process, there is a grain structure, evident in the AFM and SEM pictures in Figure 1, that would reduce by scattering the transmittance of the LIPSS structures at visible and near UV wavelengths.[37] Other effects like lattice deformation or band bending associated with defects may also contribute to the observed deformation of the absorption edge.[43]

A direct comparison of our optical transmittance results with those in refs. [15,16] is hampered by the spectral interval (visible range only) where measurements are provided in those references. For what concerns the VIS range, our results are in general similar to those on refs. [15,16] (high transmission) due to the fact that the optical bandgap of the material is in itself not strongly modified by the compositional changes observed, and is more affected, as above indicated, by grain boundary scattering near the band-edge. In near IR, when compared to the reflectance results included in ref. [17], it is worth noting that we do not observe dichroism in the LF-samples, which in addition show larger near IR reflectance, likely because only small compositional changes are induced in the LF processed structures in our case.

2.4. Electrical Properties of the Irradiated Surfaces

The analysis of the optical properties of the LF and HF samples already provides a strong indication that the processed

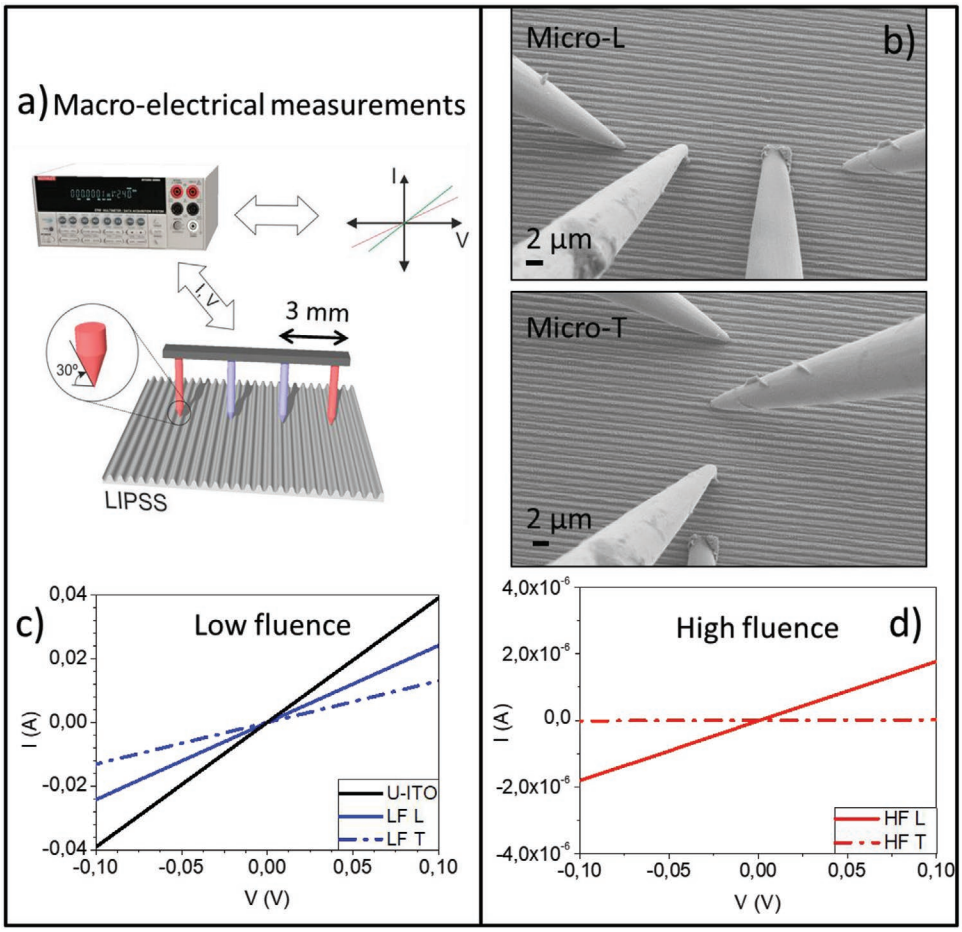

Figure 7. a,b) Experimental layout used for the four-point probing resistivity measurements. The current is measured at the outermost electrodes. In the macro-configuration (a,c), the electrode separation is fixed (3 mm). In the micro-configuration measurements (b,d), the actual distance between the electrodes is determined from SEM images. c,d) *I*–*V* curves measured for the LF samples in the macro-configuration and HF samples in the micro-configuration for the electrodes aligned longitudinally (L) or transversally (T) to the LIPSS direction. The *I*–*V* curve of an unexposed film is included for reference. In the micro-scale measurements, tips are carefully located at the ridges of the structures.

surfaces remain conductive, as deduced from their low near IR transparency, linked to the presence of free carriers. Electrical properties have been investigated by the four-point probe method either in a macroscopic or a micro-scale configuration, as sketched in **Figure 7**a. In both cases, measurements were performed with the probes aligned either longitudinally or transversally to the LIPSS.

Figure 7c,d show several *I*–*V* curves obtained for the LF and HF samples. In the LF case, the *I*–*V* measured curves show slope values in the 10^{-1} Ω^{-1} range, very similar to those of the pristine material. However, as it can be seen in Figure 7c, the slope of the *I*–*V* curve is a factor ≈2 higher for the L configuration than for the T one. From these features, we can extract two important conclusions: a) the conductivity of the whole surface is preserved both at the macroscopic and microscopic scales; b) the effective resistivity of the surface, as expected from the morphology of the surface structures, is strongly anisotropic (a conductivity anisotropy factor of ≈2). It is worth noting that the fine modulation depth perpendicular to the field of the laser that is observable in the AFM image in Figure 1a, does not cause electrical insulation since otherwise macroscopic *I*–*V* measurements would yield negligible intensity measurements.

In the HF case, the anisotropy is much more pronounced though. The *I*–*V* curves in the micro-scale (Figure 7d) show that the material is still conductive along the longitudinal direction but insulating in the transversal one. Yet, the slope of the *I*–*V* curve is four orders of magnitude smaller than in the pristine film, likely as a consequence of the combined effect of thickness diminution and compositional and structural changes. For these samples, the macroscopic measurements show no measurable current values with the probes oriented in either direction, something that can be attributed to the presence of discontinuities along the ridges of the LIPSS (cf. Figure 1). The values shown in Figure 7d are thus representative of the behavior of the HF-LIPSS in the absence of such local discontinuities that, as above indicated, are related to the build-up of thermal stresses and irregularities in the repetitive melting-solidification process at HF.

In the previous paragraphs, we have not provided resistivity parameters because to obtain the resistivity (ρ) and sheet resistance (Ω sq^{-1}) from the *I*–*V* curves a homogeneous film thickness has to be assumed. We have used a simplified model, depicted in **Figure 8**, to estimate the corresponding effective parameters

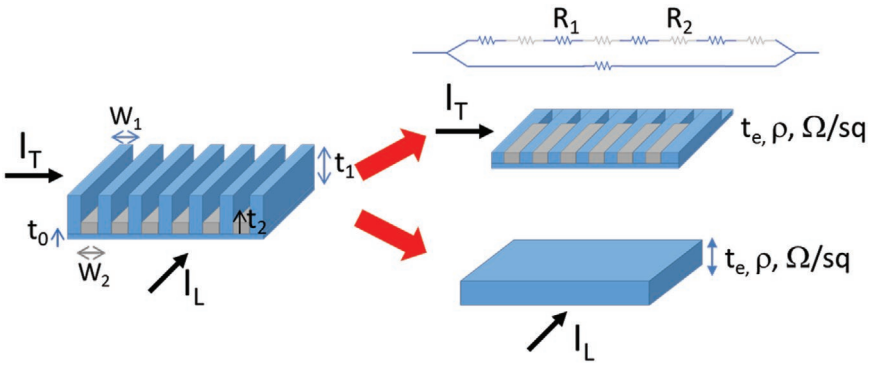

Figure 8. Sketch of the electrical circuits equivalent to the laser-induced structures when resistivity is measured longitudinally or transversally to the LIPSS direction (see text).

of the irradiated material. It can be modeled as an equivalent circuit with multiple resistances as long as its total thickness is smaller than approximately half of the probe spacing.[44]

The structure is modeled as a periodic array of stripes of two materials, with different width and thickness, and high or low sheet resistance. The stripes are placed on top of a layer of unmodified material. When current is measured in the L configuration, the electrons flow mainly through the low resistance stripes and the unmodified ITO layer. The equivalent circuit is then defined by a film with an effective resistivity and an equivalent thickness. For the T case, the equivalent circuit is a set of alternating resistances with high and low values in parallel to a resistance "made" of pristine ITO. **Table 2** shows the calculated effective resistivity parameters of the samples. Geometric and material parameters used for the calculation are given in Table S2, Supporting Information.

The unexposed material shows resistivity parameters consistent both with the transmission spectra[37] in Figure 6 and the deposition technique used.[38] In the LF case, for the L measurements, the smaller thickness at the valleys yields an effective thickness (≈400 nm), smaller than the initial film thickness. This generates a slight increase of ρ_L with respect to the pristine material value (from 5.6×10^{-4} to 7.5×10^{-4} Ω·cm). However, the relevant parameter in terms of material properties, $(\Omega\ sq^{-1})_L$, still shows a low value (<20 Ω) which indicates that the sheet resistance of the material at the valleys must be close to that of pristine ITO. This is confirmed by the measured ρ_L values that show resistivity values similar to those of the non-irradiated material. Since in this case the equivalent thickness is mostly given by the thickness at the valleys of the LIPSS, the derived sheet resistance $(\Omega\ sq^{-1})_T$ shows a stronger increase with respect to the initial material.

Globally, these estimates show that the material at the ridges and valleys of the LIPSS in the LF sample has a sheet resistance rather similar to that of as-deposited ITO, and that the effective resistivity parameters found are more conditioned by the aspect ratio of the LIPSS than by compositional changes. From this, it can be also concluded that the use of a multi-scan approach (repeating the structuring process at LF several times) should enable generating structures where the material at the ridges preserves (nearly unaltered) its thickness and composition while the material at the valleys is completely removed. This would lead to structures behaving as insulating in the direction transverse to the LIPSS and behaving as pristine ITO in the longitudinal one. Such ultrahigh performance anisotropic TCE surfaces would find a wealth of applications, for instance, in conductive flexible paths (ACFs), electrolytes in Li-ion batteries, or catalysis.[45,46]

For the HF case, as expected from the large width, and negligible thickness of the material remaining at the valleys, the structure is insulating in the direction transversal to the LIPSS. The strong increase (four orders of magnitude above pristine ITO) in sheet resistance in the parallel direction can be mostly ascribed to the strong increase in the Sn/In ratio, now apparently occurring throughout all the remaining material, and not only in the near-surface region. As above indicated, with the estimation of the Sn/In (at%) derived from the XPS measurements, a carrier density below 10^{20} cm^{-3} in the material remaining at the LIPSS maxima should be expected. It is worth noting that despite this, the material is still simultaneously conductive and transparent for visible wavelengths and shows a huge anisotropy. The resistivity of the structure (≈1 Ω·cm) is in the level required for interfacial buffer layers for bulk

Table 2. Equivalent thickness, resistivity (ρ), and sheet resistance ($\Omega\ sq^{-1}$) values estimated from the model for the LF and HF samples derived from macro- and micro-configuration, four-point probing measurements (FPP) for the L and T measurement configurations.

Process	FPP	Direction	Eq. thickness [nm]	ρ [Ω·cm]	Ω/sq [Ω]
Unexposed	Macro	NA	500	5.2×10^{-4}	11.20
LF	Macro	L	408	7.7×10^{-4}	18.76
LF	Macro	T	150	5.2×10^{-4}	34.70
HF	Micro	L	45	9.5×10^{-1}	208 702
HF	Micro	T	10	Insulating	Insulating

heterojunction organic solar cells[47] or can find application in the growth of anisotropic aligned nanostructures.[48]

For what concerns the comparison between optical and electrical properties, the behavior observed in both types of properties seems fully consistent once the role of the Sn/In ratio in the density of free carriers and their mobility is considered. Modeling of the propagation of the electromagnetic field through the structures using finite-difference time-domain simulations, like those reported in ref. [16] in fs-laser irradiated ITO films, would enable a more quantitative analysis. It must be noticed though, that in this reference it is assumed that the optical properties of the material remaining in the LIPSS corresponds to pristine ITO, something we must discard in our case, at least in the HF-samples. This would strongly hinder the achievement of reliable values from simulation.

3. Conclusion

We have designed a route for producing strongly anisotropic resistivity surfaces by fs-laser processing of ITO films. The process is based on the formation and coherent propagation of LSF-LIPSS over cm^2-sized regions at high processing speed. Depending on the laser fluence used, two types of anisotropic resistivity structures can be produced. At relatively high laser fluences, coherently extended, ablative ripples are produced with a strong diminution of the whole film thickness and a modulation depth in the LIPSS reaching the film-substrate interface. The material remaining at the ridges shows though, a strong increase in its Sn/In compositional ratio. As a consequence, the produced structure is insulating along the direction transverse to the LIPSS and shows a resistivity, $\rho_L \approx 1.0\ \Omega\cdot$cm for the longitudinal direction. These HF structures are also strongly dichroic in the near-IR. At lower fluences, shallower ablation is induced at the valleys of the ripples, while there is a nearly negligible material loss at their ridges. These structures show a resistivity $\rho_T \approx 10^{-3}\ \Omega\cdot$cm along the LIPSS direction, close to that of the pristine film, while ρ_T increases by a factor of ≈2. Multi-scan processing at LF would enable producing structures behaving as insulating in the direction transverse to the LIPSS and behaving as pristine ITO in the longitudinal one. The basis for the development of ultrahigh performance anisotropic TCE surfaces based on ITO has therefore been established. There are two aspects worth emphasizing at this point. The first is the fact that the approach consisting of the fabrication of anisotropic TCE surfaces by laser-induced, self-organized structuring could be applied to other transparent conductors based on materials less scarce than In. The second is the fact that, even for the case of ITO, there are niche applications as electrochemical sensors, optical electroswithching, etc. where the consumption of ITO (by the use of a subtractive process) would be comparatively very little and where the cost (due to the scarcity in the supply) would be perfectly assumed in the price of the final products. For some of these applications, the chemical stability of ITO in water and water solutions (e.g., in biological fluids) is a decisive factor in its choice for these applications. In this regard, it is noteworthy that the availability of laser patterning methods compatible with any kind of substrate would constitute a breakthrough to improve the device response and/or to increase sensitivity.[49,50]

4. Experimental Section

Polycrystalline ITO films on fused silica substrates were used for the laser structuring experiments. They were fabricated by RF magnetron sputtering deposition using a power of 50 W and a bias of 175 V in Argon atmosphere (5×10^{-3} mbar) with a sample holder kept at 350 °C. An X-ray diffractogram of an as-deposited, polycrystalline film was included in Figure 1. Their thickness was 500 nm and their resistivity $\rho = 5.5 \times 10^{-4}\ \Omega\cdot$cm (11 Ω sheet resistance).

Structuring was performed using an Yb-fiber femtosecond laser amplifier (Satsuma HP), delivering 350 fs pulses at $\lambda = 1030$ nm, with a repetition rate that was varied in the 50–500 kHz range. The linearly polarized laser beam entered a galvanometric scanner equipped with an F-Theta lens (100 mm focal length) and was focused to a size of 10.2 µm ($1/e^2$ intensity decay), leading to local fluences in the 0.5–3.0 J cm^{-2} range. Regions of 1×1 cm^2 were irradiated using beam scanning speeds in the 0.1–2 m s^{-1} range, with a separation between scan lines in the 4–12 µm range. The beam polarization was aligned, in most cases, perpendicularly to the scanning direction to facilitate to coherent extension of LIPSS.[16,17] A parallel configuration was also explored in some samples.

The surface morphology of the structures was first inspected by optical microscopy with monochromatic illumination at 460 nm. Scanning electron microscopy (SEM) was performed with a HITACHI S4800 field emission microscope operating at 2 kV in secondary electron (SE) and backscattered electron (BSE) modes. Some of the pristine and laser-irradiated samples were cleaved (transversally to the LIPSS) and their cross-sectional morphology analyzed by SEM, as shown in Figure 1. Atomic force microscopy (AFM) images were obtained using the tapping mode of a Nanotec microscope with Dulcinea electronics, and then analyzed with the WSxM software.[51] Depth profiles of the surfaces were also measured with a Sensofar S-Neox confocal-interferometric optical microscope which has a 20 µm maximum vertical scanning range, 1 µm display resolution, and 2 nm vertical resolution working in white light mode at 50×.

Optical properties were studied by means of a Perkin Elmer Lambda 750 UV–vis–NIR spectrophotometer. The illumination beam for the optical transmittance measurements was un-polarized and reached the sample at normal incidence. Spectra of processed samples with their LIPSS oriented either parallel or perpendicular to the lines of the diffraction grating of the spectrophotometer were acquired to analyze the presence of dichroism in the laser-processed structures.

Compositional changes were analyzed by Energy Dispersive X-Ray Analysis (EDX) spectra registered with a Bruker-X Flash-4010 analyzer working at 20 kV installed in same SEM system above described. Surface chemical composition was also analyzed by X-ray photoelectron spectroscopy (XPS) at normal incidence using the AlKα line to excite the spectra. These were calibrated using the C1s peak associated with adventitious carbon surface contamination at 284.5 eV. The crystalline structure of the material was analyzed by glancing angle X-Ray Diffraction (XRD) in a Panalytical X'PERT PRO diffractometer working at an angle of incidence of 0.2°. Additionally, thin lamellae of pristine and LF irradiated samples were produced using a FIB. The cross-section lamellae were fabricated by FIB in a Zeiss Auriga CrossBeam Workstation. First, a lamella of 5 µm was shaped by FIB using a gallium etching source and fixed with Pt to the Cu grid. Then, the lamella was thinned to a thickness of 50–70 nm using 600, 240, 120, and 50 pA and 30 kV conditions. The cross-sectional samples were characterized by HAADF-STEM in a FEI Talos F200S microscope equipped with a 2SDD EDX system working at 200 kV.

Finally, electrical resistivity measurements were performed by the four-point probe method with a Keithley 2635A System Source Meter. The electrodes (Macro RS Pro with 2.54 mm pitch spring probes) were phosphor bronze needle tips of 24.7 mm length, 1.03 mm diameter, and 30° angle, with a separation of 3 mm among them. Additional electrical measurements at the micro-scale were performed in a Zeiss Gemini 300 SEM microscope equipped with a Kleindiek micromanipulators system and an electron beam induced current detector. For the four-point probe measurements, a set of Micro-Pico Probes T4-10 made of tungsten with 3.3 mm length, 10 µm diameter, and <0.1 µm point radius was used.

Supporting Information

Supporting Information is available from the Wiley Online Library or from the author.

Acknowledgements

This research was funded by the Spanish Ministry of Science, Innovation and Universities, the Spanish Research Agency (AEI, Ministry of Research and Innovation), and the European Regional Development Fund (ERDF) (grant numbers TEC2017-82464-R, PID2019-109603RA-I00, and PID2019-110430GB-C21), the "Consejería de Economía y Conocimiento de la Junta de Andalucía" (PAIDI-2020 projects P18-RT-3480 and -6079). The authors also acknowledge the Consejo Superior de Investigaciones Científicas for the "Intramural Project" (201850E057). C.L.-S. acknowledges the funding of the University of Seville through the "VI Plan Propio de Investigación y Transferencia de la US" (VI PPIT-US). M.M.-M. acknowledges the postdoctoral Juan de la Cierva Incorporación grant (IJCI-2017-33317)) of the same ministry. C.F. thanks the support from the European Commission through the Marie Curie Global Fellowship grant number 844977. V.L.-F. thanks the support from European Commission/Junta de Andalucía Talent-Hub Program. The authors thank the Research, Technology, and Innovation Center of the University of Seville (CITIUS) and Microscopy Service of the University Pablo de Olavide (Seville) for access to several material characterization facilities.

Conflict of Interest

The authors declare no conflict of interest.

Keywords

anisotropy, fs-laser processing, indium tin oxide, laser-induced periodic surface structures, resistivity, transparent conductive oxides

Received: June 29, 2020
Revised: October 25, 2020
Published online: November 23, 2020

[1] K. Ellmer, *Nat. Photonics* **2012**, *6*, 809.
[2] K. L. Chopra, S. Major, D. K. Pandya, *Thin Solid Films* **1983**, *102*, 1.
[3] O. Yavas, M. Takai, *Appl. Phys. Lett.* **1998**, *73*, 2558.
[4] J. Wang, F. Lisco, D. A. Hutt, L. C. R. Jones, J. W. Bowers, P. J. M. Isherwood, Z. Zhou, P. P. Conway, *Mater. Des.* **2020**, *194*, 1.
[5] T. Park, D. Kim, *Thin Solid Films* **2015**, *578*, 76.
[6] T. Königer, T. Rechtenwald, I. Al-Naimi, T. Frick, M. Schmidt, H. Münstedt, *J. Coat. Technol. Res.* **2010**, *7*, 261.
[7] C. McDonnell, D. Milne, H. Chan, D. Rostohar, G. M. O'Connor, *Opt. Lasers Eng.* **2016**, *80*, 73.
[8] O. Yavas, M. Takai, *J. Appl. Phys.* **1999**, *85*, 4207.
[9] H. Z. Yang, G. D. Jiang, W. J. Wang, X. S. Mei, A. F. Pan, Z. Y. Zhai, *Appl. Phys. B: Lasers Opt.* **2017**, *123*, 251.
[10] G. Račiukaitis, M. Brikas, M. Gedvilas, T. Rakickas, *Appl. Surf. Sci.* **2007**, *253*, 6570.
[11] H. W. Choi, D. F. Farson, J. Bovatsek, A. Arai, D. Ashkenasi, *Appl. Opt.* **2007**, *46*, 5792.
[12] S. Krause, P. T. Miclea, F. Steudel, S. Schweizer, G. Seifert, *EPJ Photovoltaics* **2013**, *4*, 40601.
[13] J. Zhao, X. Ding, J. Miao, J. Hu, H. Wan, S. Zhou, *Nanomaterials* **2019**, *9*, 203.
[14] J. Bonse, S. Hohm, S. V. Kirner, A. Rosenfeld, J. Kruger, *IEEE J. Sel. Top. Quantum Electron.* **2017**, *23*, 9000615.
[15] C. Wang, H.-I. Wang, C.-W. Luo, J. Leu, *Appl. Phys. Lett.* **2012**, *101*, 101911.
[16] A. Cerkauskaite, R. Drevinskas, A. Solodar, I. Abdulhalim, P. G. Kazansky, *ACS Photonics* **2017**, *4*, 2944.
[17] N. Charipar, R. C. Y. Auyeung, H. Kim, K. Charipar, A. Piqué, *Opt. Mater. Express* **2019**, *9*, 3035.
[18] A. Solodar, A. Cerkauskaite, R. Drevinskas, P. G. Kazansky, I. Abdulhalim, *Appl. Phys. Lett.* **2018**, *113*, 081603.
[19] A. Ruiz De La Cruz, R. Lahoz, J. Siegel, G. F. De La Fuente, J. Solis, *Opt. Lett.* **2014**, *39*, 2491.
[20] Y. Fuentes-Edfuf, M. Garcia-Lechuga, D. Puerto, C. Florian, A. Garcia-Leis, S. Sanchez-Cortes, J. Solis, J. Siegel, *Sci. Rep.* **2017**, *7*, 4594.
[21] M. Afshar, M. Straub, H. Voellm, D. Feili, K. Koenig, H. Seidel, *Opt. Lett.* **2012**, *37*, 563.
[22] C. Wang, H.-I. Wang, W.-T. Tang, C.-W. Luo, T. Kobayashi, J. Leu, *Opt. Express* **2011**, *19*, 24286.
[23] N. Farid, P. Dasgupta, G. M. O'connor, *J. Phys. D: Appl. Phys.* **2018**, *51*, 155104.
[24] P. Liu, W. Wang, A. Pan, Y. Xiang, D. Wang, *Opt. Laser Technol.* **2018**, *106*, 259.
[25] A. Pan, W. Wang, B. Liu, X. Mei, H. Yang, W. Zhao, *Mater. Des.* **2017**, *121*, 126.
[26] H. M. Reinhardt, P. Maier, H. Kim, D. Rhinow, N. Hampp, *Adv. Mater. Interfaces* **2019**, *6*, 1900401.
[27] C. W. Cheng, I. M. Lee, J. S. Chen, *Appl. Surf. Sci.* **2014**, *316*, 9.
[28] C. Donley, D. Dunphy, D. Paine, C. Carter, K. Nebesny, P. Lee, D. Alloway, N. R. Armstrong, *Langmuir* **2002**, *18*, 450.
[29] B. D. Darwent, *Bond Dissociation Energies in Simple Molecules*, Vol. *42*, National Standard Reference Data Series, National Bureau of Standards, Gaithersburg, MD **1965**.
[30] R. L. Weiher, R. P. Ley, *J. Appl. Phys.* **1966**, *37*, 299.
[31] F. J. Arlinghaus, *J. Phys. Chem. Solids* **1974**, *35*, 931.
[32] P. D. C. King, T. D. Veal, F. Fuchs, C. h. Y. Wang, D. J. Payne, A. Bourlange, H. Zhang, G. R. Bell, V. Cimalla, O. Ambacher, R. G. Egdell, F. Bechstedt, C. F. Mcconville, *Phys. Rev. B: Condens. Matter Mater. Phys.* **2009**, *79*, 205211.
[33] O. Bierwagen, *Semicond. Sci. Technol.* **2015**, *30*, 024001.
[34] J. H. W. De Wit, *J. Solid State Chem.* **1975**, *13*, 192.
[35] S. M. Eaton, H. Zhang, P. R. Herman, F. Yoshino, L. Shah, J. Bovatsek, A. Y. Arai, *Opt. Express* **2005**, *13*, 4708.
[36] J. R. Bellingham, W. A. Phillips, C. J. Adkins, *J. Phys.: Condens. Matter* **1990**, *2*, 6207.
[37] Y. Hu, X. Diao, C. Wang, W. Hao, T. Wang, *Vacuum* **2004**, *75*, 183.
[38] Y. Shigesato, S. Takaki, T. Haranoh, *J. Appl. Phys.* **1992**, *71*, 3356.
[39] Y. Shigesato, D. C. Paine, *Appl. Phys. Lett.* **1993**, *62*, 1268.
[40] T. Maruyama, K. Fukui, *J. Appl. Phys.* **1991**, *70*, 3848.
[41] Y. a.-H. Tseng, H. Yang, C.-W. Luo, *Opt. Express* **2017**, *25*, 33134.
[42] I. Hamberg, C. G. Granqvist, *J. Appl. Phys.* **1986**, *60*, R123.
[43] D. Mergel, Z. Qiao, *J. Appl. Phys.* **2004**, *95*, 5608.
[44] Y. u.-Y. i. Chen, J.-Y. Juang, *Meas. Sci. Technol.* **2016**, *27*, 074006.
[45] M. Yoshio, T. Kagata, K. Hoshino, T. Mukai, H. Ohno, T. Kato, *J. Am. Chem. Soc.* **2006**, *128*, 5570.
[46] Q. Wan, E. N. Dattoli, W. Y. Fung, W. Guo, Y. Chen, X. Pan, W. Lu, *Nano Lett.* **2006**, *6*, 2909.
[47] A. K. Chu, W. C. Tien, S. W. Lai, H. L. Tsai, R. Y. Bai, X. Z. Lin, L. Y. Chen, *Org. Electron.* **2017**, *46*, 99.
[48] J. Parra-Barranco, F. J. García-García, V. Rico, A. Borrás, C. López-Santos, F. Frutos, A. Barranco, A. R. González-Elipe, *ACS Appl. Mater. Interfaces* **2015**, *7*, 10993.
[49] I. Ashur, A. K. Jones, *Electrochim. Acta* **2012**, *85*, 169.
[50] R. Pruna, M. López, F. Teixidor, *Nanoscale* **2019**, *11*, 276.
[51] I. Horcas, R. Fernández, J. M. Gómez-Rodríguez, J. Colchero, J. Gómez-Herrero, A. M. Baro, *Rev. Sci. Instrum.* **2007**, *78*, 013705.